Applied Physics A (2023) 129:588
https://doi.org/10.1007/s00339-023-06839-z

Applied Physics A
Materials Science & Processing

DC sputtered $ZrO_2/Zn_{(1-x)}Sn_{(x)}O$ thin-film transistors and their property evaluation

Prashant Bhat[1] · Parashurama Salunkhe[1] · Dhananjaya Kekuda[1]

Received: 10 May 2023 / Accepted: 13 July 2023 / Published online: 28 July 2023
© The Author(s) 2023

Abstract
A bottom gate staggered 30 nm $Zn_{(1-x)}Sn_{(x)}O$ ($x = 0.14$) (TZO)-based thin-film transistors (TFTs) were fabricated using DC magnetron reactive sputtering method. Highly transparent 120 nm dc sputtered ZrO_2 was used as a gate dielectric. The oxygen flow rate was varied from 20 to 24% during channel layer (TZO) coating and its effect on structural, morphological, optical, chemical, and electrical parameters were systematically studied. A nano scale roughness was noticed by atomic force microscopy (AFM), and ultra-smooth nature in root mean square roughness (RMS) was observed with an increment in the oxygen flow ratio. The increase in the oxygen-related defects with increase in the oxygen flow ratio in channel layer was evident from X-ray photoelectron spectroscopy (XPS). The electrical characterization of gate dielectric was carried out for Al–ZrO_2–Al structure. The high capacitance density ~ 121.9 nF/cm^2 for 120 nm ZrO_2 was obtained from the capacitance–voltage (C–V) measurement. The fabricated TFTs operated in n-channel depletion mode and indicated pinch-off region at lower source–drain voltages. In addition, the transfer characteristics of TFTs confirmed I_{on}/I_{off} ratio of 10^5, with a field effect mobility of 23 cm^2/V.s. This low temperature processed TFT unlocks the possibility of use in the next generation foldable display technology.

Keywords ZnO · TZO · ZrO_2 · Thin-film transistors · Oxygen flow ratio · Levinson plot

1 Introduction

Thin-film transistors (TFTs) have been extensively studied in recent years by several researchers due to their potential applications in power electronics, display technology, RFID integrated circuits, and other fields [1]. The selection of suitable ionic semiconductors is critical in achieving desired device performance. The material properties such as high carrier mobility and high optical transparency are most crucial for achieving enhanced device performance. In addition, materials that can be processed using low-temperature synthesis techniques ensures scalability for large-scale device fabrication [2]. Hoson et al. [3] created the first breakthrough TFT in 2004 based on indium–gallium–zinc oxide (IGZO), which were employed in display technology and memory applications due to high electron mobility and low voltage consumption. However, the toxicity nature of indium along with high material cost and elemental scarcity, makes it imperative for finding other alternatives. Among the possible replacements, such as ZnAlO, MgZnO, and ZnSnO [4], ZnSnO is the most popular ones due to the low-cost, non-toxic and earth-abundant nature. Recently, TFTs fabricated with zinc–tin–oxide active channel layers have been demonstrated to have excellent electrical performance comparable to IGZO-based TFTs [5–7]. It is noteworthy that for best performing TFTs, a gate oxide layer with a high dielectric constant (k) is essential. However, the majority of TFTs use SiO_2 as a gate dielectric material, which has lower dielectric constant (k), requires a higher power supply for operation and optically opaque. Recent trend in display technology is active-matrix–organic light emitting (AMOLED) panels which calls for transparent gate dielectric layers with higher dielectric constant (k). Henceforth, transparent dielectric layers that have high capacitance density with lower leakage current at significantly low thicknesses are gaining the attention [8–12]. High-k binary oxides include Ta_2O_5 [13], Y_2O_3 [14], TiO_2 [15], Al_2O_3 [16], HfO_2 [17], and ZrO_2 [18–22] etc., which are potential candidates

✉ Dhananjaya Kekuda
dhaya.kekuda@manipal.edu

[1] Department of Physics, Manipal Institute of Technology, Manipal Academy of Higher Education, Manipal 576104, India

for transparent gate dielectric layers in TFTs. Among these binary oxide dielectric materials, ZrO_2 is notable for its high dielectric constant (~ 16) and optical transparency (transmittance > 85%), low processing temperature (< 200 °C) and significant thermal stability. In addition to these properties, ZrO_2 also has a high band offset with prominent large bandgap oxide semiconductors such as ZnO, SnO_2, NiO, and others used for TFT applications. Chiu et al. [23] worked on IGZO-based TFTs, they observed current on–off ratio about 10^3, and field effect mobility of 18 cm^2/Vs with a threshold voltage of 1 V. Li et al. [24] observed current on–off ratio about 10^4 and threshold voltage of 0.94 V in IZO-based TFTs, likewise R. Navamathavan et al. [25] reported current on–off ratio about 10^5 and field effect mobility of 34 cm^2/Vs in ZnO-based TFTs. There have been many articles on the production of pristine and doped ZnO thin films utilising different deposition processes, such as pulsed laser deposition [13], sputtering [14, 15], chemical vapour deposition [16], sol–gel method [17], and so on. Among these techniques we selected of reactive sputtering method in the present work, because sputtering technique is industrially recommended method for most device fabrications. Moreover, it possess main advantages, such as (i) low processing growth temperature, (ii) good adherence to substrate, (iii) high deposition rate, and (iv) improved control over scaling to a vast area [26–29]. It is well-known that to synthesize the gate dielectric layers, radio frequency (RF) sputtering with ceramic targets has been the most popular technique [30]. However, the method is not cost-effective and can be replaced with direct current (DC) reactive magnetron sputtering, which also offers a higher deposition rate with better film uniformity and the option of using metal targets, which are significantly less expensive to produce than ceramic targets [2]. This work proposes respective novel aspects in the field of thin-film transistors (TFTs). It explores $Zn_{(1-x)}Sn_{(x)}O$ ($x = 0.14$) (TZO)/ZrO_2 TFTs, employing ZrO_2 as a transparent gate dielectric layer. The impact of oxygen flow ratio during TZO thin-film deposition on TFT performance is examined. Moreover, the study substitutes ceramic targets with metal targets in the fabrication process using direct current (DC) reactive magnetron sputtering. These influences offer new understandings and potential advancements in TFT design, addressing issues related to material toxicity, cost and scalability.

2 Experimental details

2.1 TFT fabrication

$Zn_{(1-x)}Sn_{(x)}O$ (TZO) and Zirconium oxide (ZrO_2) thin films were synthesized using direct current (DC) magnetron reactive sputtering on a glass substrate. A standard substrate cleaning procedure and can be found in elsewhere [31]. To get a base vacuum of 9.8×10^{-4} Pa the diffusion pump was used, which was assisted by a rotary pump. High pure (99.99%) metallic targets of Zn, Sn and Zr were used for the coating. To control the flowrate of argon and oxygen, individual mass flow controllers (ALICAT Scientific) were used, and the working pressure was maintained about 0.9 Pa. For performing co sputtering of Zn and Sn, two independent power supplies were used, and sputtering power was fixed about 35W for Zn and 6W for Sn metallic targets. Similarly, for the deposition of ZrO_2, the 100W power was maintained for Zr metallic target. Initially to check the leakage current and the capacitance of the dielectric material (ZrO_2) metal–insulator–metal (MIM) architecture was constructed by sandwiching the ZrO_2 layer in between Aluminum (Al) electrodes. The top and bottom Al contacts of ultra-thin 120 nm were thermally evaporated. Later to construct the TFT device, patterned Al electrode were made on glass substrate for gate contact by utilizing thermal evaporation technique. On the top of these patterned gate electrodes, the ZrO_2 having the thickness of 120 nm was coated using DC magnetron reactive sputtering method. The $O_2/(O_2 + Ar) \times 100$ flow ratio was maintained at about 15.38% for ZrO_2 coating. Later the active channel layer magnetron sputtered (TZO) was synthesized at different oxygen flow ratios (i.e., at 20%, 22% and 24%) having the film thickness of 30 nm. The samples are coded, respectively, as TZO-20, TZO-22, and TZO-24. Meanwhile, ex-situ thermal air-annealing was performed at 100 °C for all the samples on a hotplate for about 20 min. Finally, thermally evaporated 120 nm source and drain contacts were made on active channel layer. In this report all the fabricated TFTs were having a fixed channel length of 30 μm and width of about 1000 μm. The detailed process flow of the constructed TFT is shown in Fig. 1a.

2.2 Characterization methods

The crystalline nature of TZO and ZrO_2 thin films was analyzed by glancing angle X-ray diffraction method (GXRD-Rigaku smart lab) with the glancing angle of 0.5 degrees. To find the elemental composition in the sample energy dispersive spectroscopy (EDS) was used [EVOMA 18 with oxford EDS (X-act)]. The thickness of the thin-film samples was measured by utilizing profilometer (Dektak XT). The surface morphology of each layer was examined by atomic force microscope (AFM-Innova SPM). To reveal the optical nature of the samples UV–visible dual beam spectrophotometer (Shimadzu UV-1800) was used. Chemical composition and oxidation states of the samples were determined using X-ray photoelectron spectroscopy (XPS) (AXIS 165 ULTRA DLD-Kartos, Analytical Limited Instrument). The instrument equipped with monochromatic

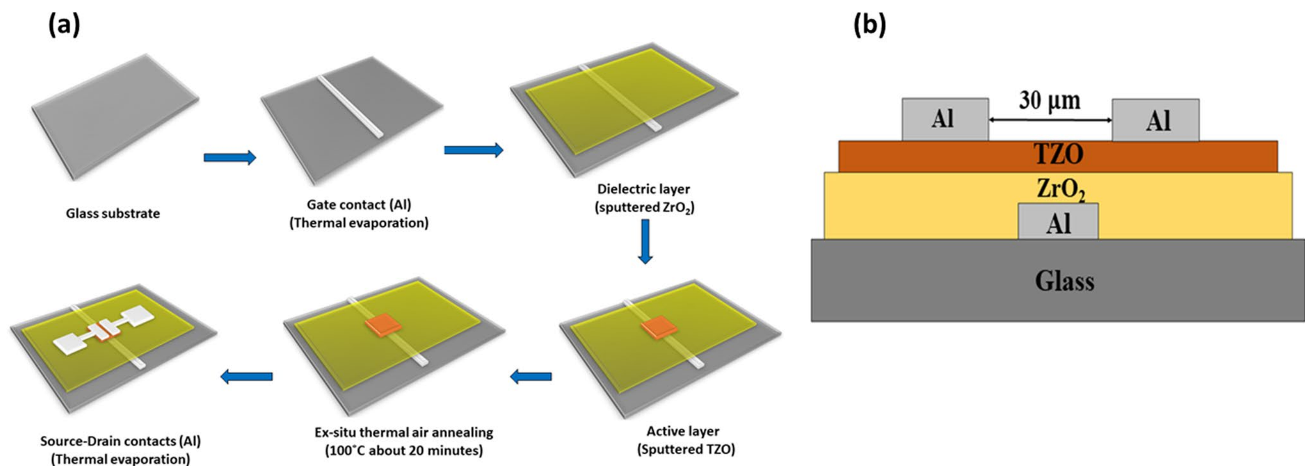

Fig. 1 Schematic of thin-film transistors (TFTs), **a** process flow of TFTs, **b** vertical view of TFT

Al $\boldsymbol{K_\alpha}$ = 1486.69eV (X-ray) source having the small spot capability of 15 microns. The vacuum before the measurement was achieved ~ 10^{-8} mbar. To avoid the broadening of XPS spectra due to charging effect an electron flood gun was used. The electrical characterization of MIM structure and TFT devices were examined by Keithley 4200-SCS and Keithley 2636 B source meter. All the devices were characterized at room temperature condition.

3 Results and discussion

3.1 Structural analysis

Figure 2 shows glancing angle X-ray diffraction patterns of both active channel layer (TZO) and dielectric layer (ZrO_2). In the XRD graph, the spectra corresponds to TZO synthesized at various oxygen flow ratio exhibits a strong c-axis orientation along (002) plane, which confirms that synthesized film is highly crystallized with highly preferred hexagonal structure and it is confirmed by JCPDS (36–1451) [31]. The tetragonal nature of ZrO_2 was also noticed in accordance with JCPDS (88–1007) [32]. To get the correlation of the dependency of the oxygen flow ratio with crystallite size using the Scherrer's formula [33]:

$$\boldsymbol{D} = \frac{0.9\lambda}{\boldsymbol{\beta}\cos\theta} \quad (1)$$

where $\boldsymbol{\lambda}$ is the wavelength of the X-ray (Cu Kα = 1.5406 Å), $\boldsymbol{\beta}$ is full-width half maximum (FWHM) of the diffraction peak and θ is known to be Bragg angle. The active layer TZO grown on 20% oxygen flow ratio has exhibited average crystallite sizes about 11.6 nm. The decrease in the crystallite sizes to 6.4 nm and 6.3 nm were observed as oxygen flow ratio

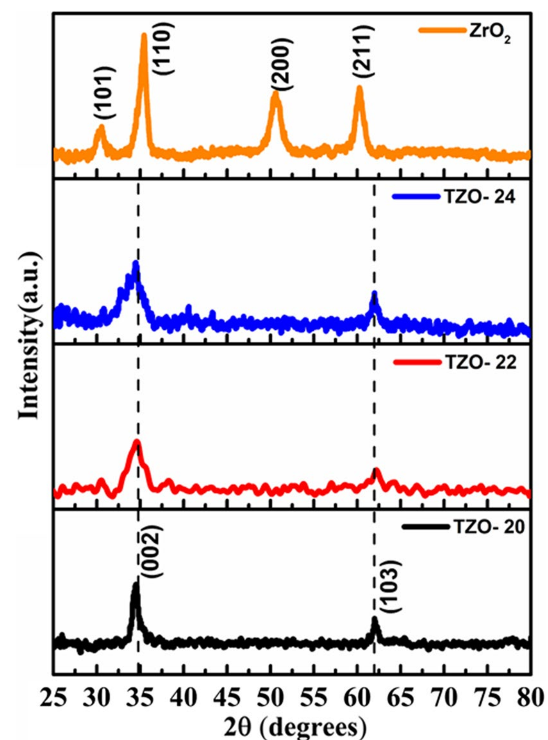

Fig. 2 Glancing angle X-ray diffraction pattern of TZO synthesized at 20%, 22% and 24% oxygen flow ratio, and ZrO_2 synthesized at 15.38% oxygen flow ratio

increased to 22% and 24%, respectively. This decrement in the crystallite sizes may be due to kinetics of sputtered film. During sputtering process, there are two main factors that affect the growth of the film, (i) bombardment of high energetic Ar^+ ions, (ii) reaction and re-sputtering of oxygen atoms. In the condition of low oxygen flow ratio bombardment of Ar^+ ions are dominant, and due to the increment in the oxygen flow

ratio, reaction rate increases compared to sputtering rate, and it develops strain in the crystal matrix consequently leading to reduction in crystallite size. To find the strain in the crystalline matrix, the following formula was used:

$$\boldsymbol{\varepsilon} = \frac{\boldsymbol{\lambda}}{\boldsymbol{D}\mathbf{sin}\boldsymbol{\theta}} - \frac{\boldsymbol{\beta}}{\mathbf{tan}\boldsymbol{\theta}} \tag{2}$$

where $\boldsymbol{\varepsilon}$ is the developed strain, and $\boldsymbol{\beta}$ is the FWHM, θ indicates the Bragg diffraction angle. The minimum strain 5.3×10^{-3} was observed in the TZO films grown on 20% oxygen flow ratio. Similarly, the strains 11.8×10^{-3} and 16.1×10^{-3} were observed for 22% and 24% oxygen flow ratio grown film, respectively. Likewise, ZrO_2 layer exhibited crystallite size of 7.7 nm with a lattice strain of about 3.5×10^{-3}. Therefore, these comparable sizes of crystallites of both active and dielectric layers could be supportive to achieve efficient thin-film device fabrication.

3.2 Surface morphology and compositional analysis

To operate the device in low operating voltage, with higher filed effect mobility smooth and defect free surface is crucial. Figure 3a–c represents the 3D AFM images of TZO samples prepared at different oxygen flow ratios. The image exhibits that all the samples have surface as homogenous, uniform, free from cracks and compact. The measured AFM in 5 µm × 5 µm area reveals the root mean square (RMS) roughness. The computed RMS value of TZO-20, TZO-22 and TZO-24 are found to be 0.62 nm, 0.34 nm, and 0.32 nm, respectively. This decrement in the RMS value of TZO film coated at different oxygen flow ratios may be due to decrease in the deposition rate with rise in the oxygen flow ratio, which gives sufficient time for the adatoms to form an ultra-smooth surface. Similarly, Fig. 3d represents the AFM image of ZrO_2 thin film, and the measured RMS roughness was found to be 0.45 nm. To find the Sn (at%) in the TZO samples and to check the distributional uniformity EDS with elemental mapping was performed. Figures 4a, 5a show the EDS spectrum. The observed cationic ratio $(Sn/(Sn + Zn) = 0.145$ for TZO-20 sample, and $(Sn/(Sn + Zn) = 0.140)$ was noticed in TZO-24 sample. Figures 4b–e, 5b–e represents the elemental mapping of TZO-20, TZO-24 and which confirms the uniform distribution of constituent elements.

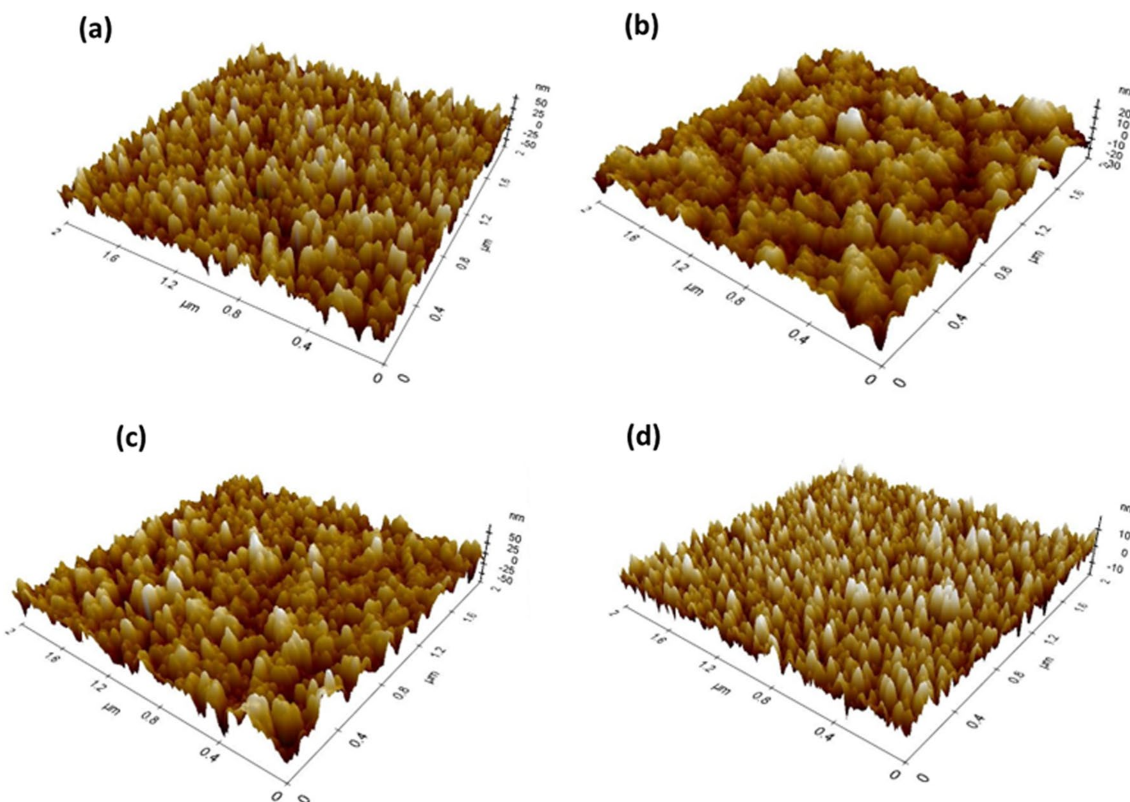

Fig. 3 AFM 3D images. **a** TZO at 20% oxygen flow ratio, **b** TZO at 22% oxygen flow ratio, **c** TZO at 24% oxygen flow ratio, **d** ZrO_2

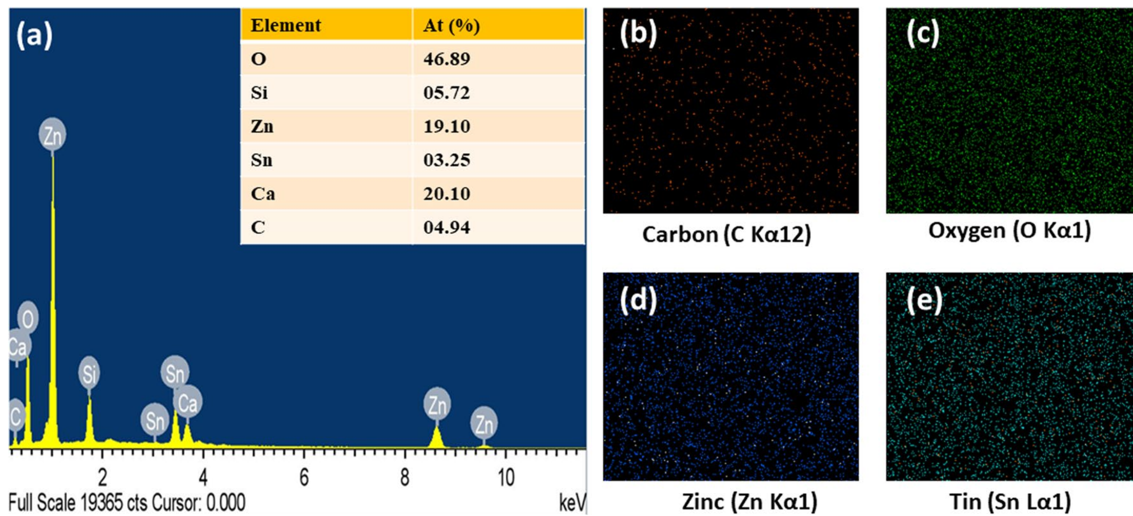

Fig. 4 EDS and elemental mapping of TZO-20. **a** EDS spectrum, **b** elemental mapping of carbon, **c** oxygen, **d** zinc, **e** tin

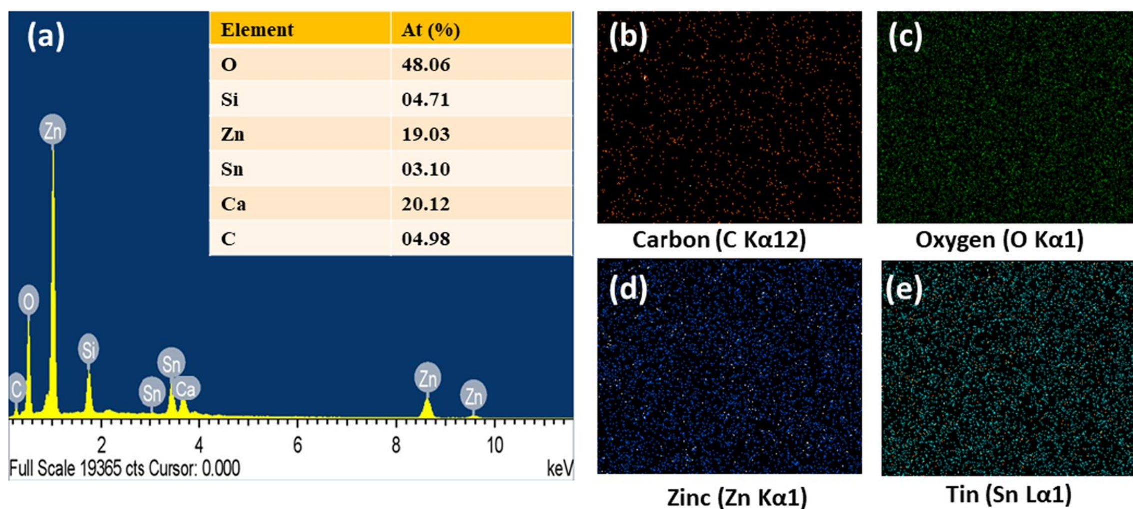

Fig. 5 EDS and elemental mapping of TZO-24. **a** EDS spectrum, **b** elemental mapping of carbon, **c** oxygen, **d** zinc, **e** tin

3.3 Optical property

Figure 6a represents the transmittance nature of the TZO samples with the inset representing the transmittance spectrum of ZrO_2 thin films. TZO film exhibited a transmittance of ~ 70% or above in the visible region. The dielectric layer has shown a transmittance of above 80% in the measured wavelength. From Fig. 6a, the interference fringes are evident in the spectrum, and it discloses that, the synthesized thin films have long range uniformity. The optical bandgap (E_g) of TZO films coated at different oxygen flow ratios was calculated by adopting standard Tauc plot for direct transition [34], by considering the intercept extrapolation line with x-axis in $(\alpha h\upsilon)^2$ versus $h\nu$ graph, as shown in Fig. 6b. The computed bandgap values are 3.42 eV, 3.40 eV and 3.30 eV for TZO-20, TZO-22, and TZO-24 samples, respectively. Similarly, the bandgap of ZrO_2 was found to be 3.96 eV (inset, Fig. 6b). The decrement in the bandgap with increase in the oxygen flow ratio for active layer could be because of the strain development in the crystal matrix. It is very important to select a gate dielectric material having good band offset with active channel layer to control the transport properties. By selecting proper band offset dielectric one can reduce the carrier injection into conduction and/or valence band of gate dielectric. Herein, the band offset of dielectric material with active channel layers were noted 0.54 eV, 0.56 eV and 0.66 eV for TZO-20, TZO-22, and TZO-24, respectively, with ZrO_2.

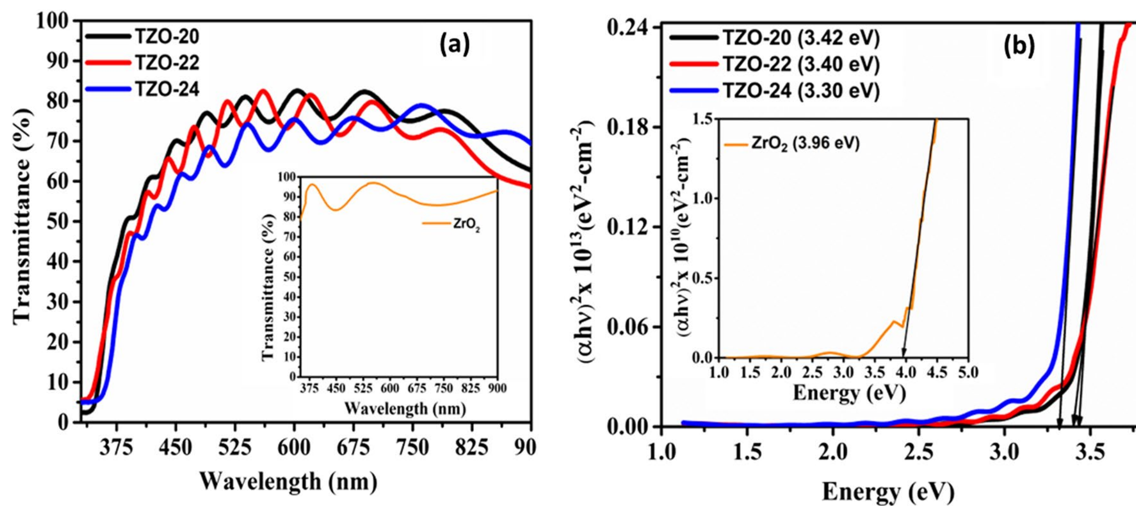

Fig. 6 Optical properties, **a** transmittance nature of TZO (inset: transmittance nature of ZrO_2), **b** optical energy bandgap of TZO (inset: optical energy bandgap of ZrO_2)

3.4 Chemical analysis

To check the chemical composition of both the active and dielectric layers XPS analyses were performed. XPS spectra were analysed with Casa XPS software, and Ar + ion etching was employed to remove surface impurities. For further investigation, the Shirley type background was applied to all the core spectra. In addition, the peaks were deconvoluted by selecting mixed Gaussian–Lorentzian fitting. Prior to measuring our samples, a calibration was performed using Au, Ag, and Cu metal samples. The measured binding energy peaks are located at 83.96 eV, 368.21 eV, and 932.62 eV, respectively, and these values are well-matched with literature [35]. According to the literature [36, 37], the standard carbon C1s peak at 284.80 eV was used for charge correction in this work for further analysis. The small and distinct satellite peaks noticed at 285.43 eV and 288.73 eV for TZO-20, 285.71 eV and 288.81 eV for TZO-24 corresponds to C–O–C and O–C=O, respectively, as shown in Fig. 7a. Figure 7b shows Zn 2p core spectra for TZO samples prepared at different oxygen flow ratios. The sample TZO-20 represents peak doublets Zn2$p_{3/2}$, Zn 2$p_{1/2}$ at 1021.48 eV and 1044.56 eV, correspondingly. Similarly, TZO-24 sample exhibits spin–orbit doublets Zn 2$p_{3/2}$ and Zn 2$p_{1/2}$ at 1021.34 eV and 1044.42 eV accordingly. Likewise, Fig. 7c shows Sn 3d core spectra of TZO samples. The sample TZO-20 characterises peak doublets Sn 3$d_{5/2}$ at 486.40 eV, Sn3$d_{3/2}$ at 494.80 eV, 498.52 eV. Moreover, TZO-24 sample exhibits spin–orbit doublets Sn 3$d_{5/2}$ at 486.30 eV, Sn3$d_{3/2}$ at 494.72 eV, 498.34 Ev, as presented in Fig. 7c. The binding energy centred at 486.40 for TZO-20 and 486.30 eV for TZO-24 samples designated that substitution of Sn^{4+} in the Zn^{2+} sites [38]. The binding energy peak centred at 494.80 eV, 498.52 eV for TZO-20 and 494.72 eV, 498.34 eV for TZO-24 in Sn 3d spectra may be corresponds SnO_2 and Zn_2SnO_4 phases, respectively, as per the literature [39]. However, diffraction peaks related to SnO_2 and Zn_2SnO_4 are not observed in the XRD analysis, so Sn doping can be interpreted as Sn ion substitution at Zn sites in the ZnO matrix. Alternatively, secondary phase formation appears to be very low in content and is thought to be lag behind the sensitivity of XRD detection. The broad as well as asymmetric O1s peaks were deconvoluted resulting in two distinct components in the TZO samples prepared at different oxygen flow ratios. Figure 7d displays O1s spectra of TZO samples, the lower binding energy peak (O_I) centred at 529.82 eV for TZO-20 and 529.55 eV for TZO-24, represents the oxygen atom connected with metal (Zn, Sn) atoms [5, 6]. The higher binding energy peak (O_{II}) centred at 531.64 eV for TZO-20 and 531.41 eV for TZO-24 is related to oxygen ions located at oxygen scarce regions inside the crystal matrix [40, 41]. Detailed information on percentage concentration of each peak in the TZO-20 and TZO-24 samples are mentioned in Table 1. The increase in the oxygen-related defects (32.59–50.42%) was noticed for increased in the oxygen flow ratio. It means that composition in the film relatively changed with the oxygen flow ratio. The binding energy of SnO and SnO_2 are smaller than that of ZnO, it is infer that that oxygen atom can combine with Sn atom relatively easier in comparison with that with Zn atom; however, increase in the oxygen flow ratio increases the oxygen vacancies. The similar behaviour was observed by Chen et al. [42] in ITO thin films. The deconvoluted Zn 2p spectra (Fig. 7b) reveals that presence of Zinc interstitials (Zn_i) at 1023.23 eV and 1023.04 eV for TZO-20 and TZO-24

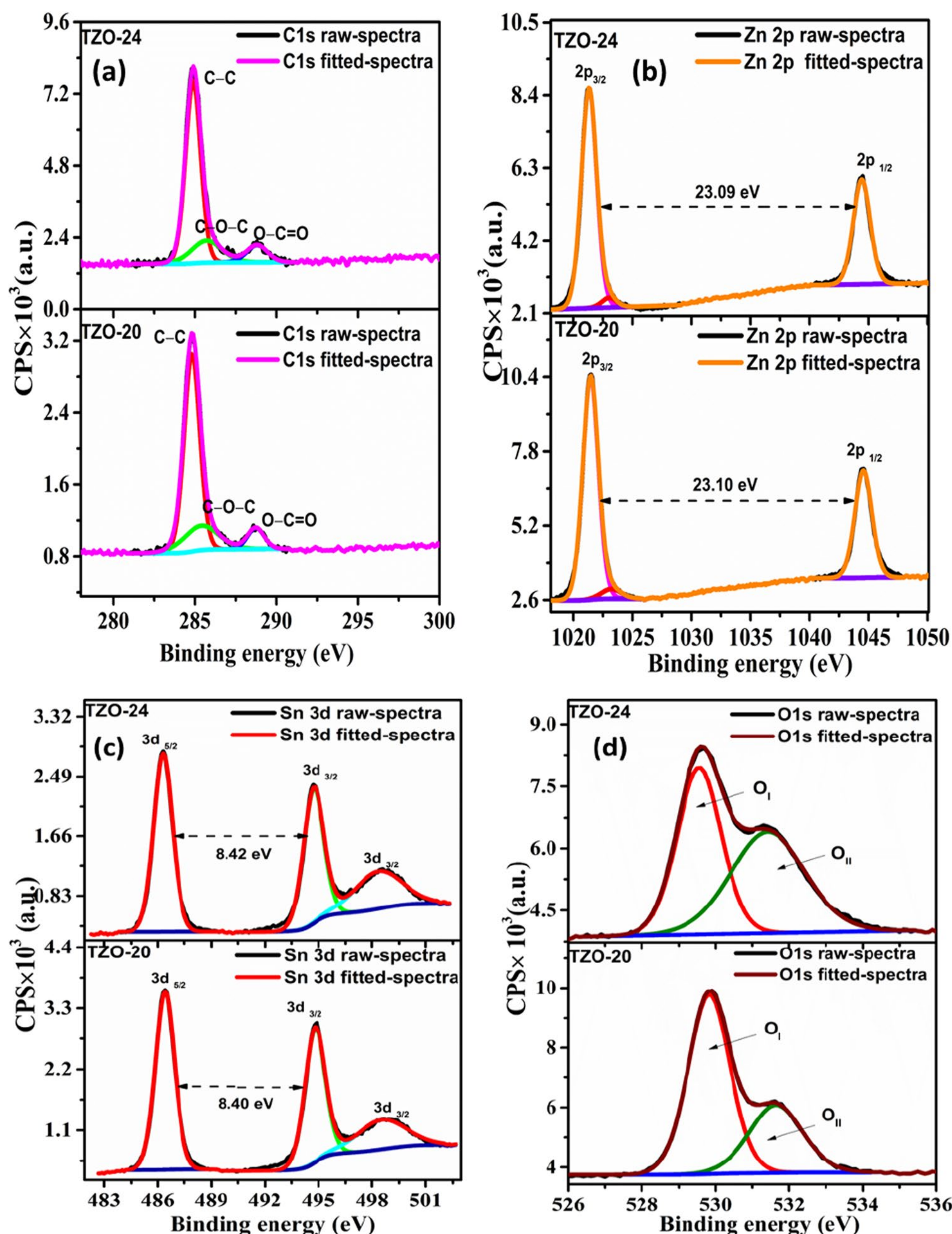

Fig. 7 XPS spectra of TZO thin films. **a** C1s spectra, **b** Zn 2p spectra, **c** Sn 3d spectra, **d** O1s spectra of TZO

samples, respectively, which decreases with respect to increase in oxygen flow ratio, as mentioned in Table 1. In general, Zn_i and Vo defects (oxygen vacancies, O_{II}) acts as trap centres and shallow donors [41], the increment in the oxygen-related defects could enhance the electrical properties of n-channel TFTs. Figure 8a shows deconvoluted C1s spectra, which represents binding energy peaks at 284.80 eV, 286.20 eV and 288.60 eV, that corresponds to C–C, C–O–C and O–C=O, respectively. Figure 8b represents the core spectra of Zr 3d, the strong spin–orbit doublet peaks were observed at 180.00 eV (59.36%) for Zr $3d_{5/2}$ and 184.38 eV (40.64%) for Zr $3d_{3/2}$. Similarly, the O1s spectra (Fig. 8c) of ZrO_2 indicates three different peaks, the first peak (O_I) at 529.72 eV (63.52%) related to oxygen ions combined with metal cations in ZrO_2, the second peak (O_{II}) at 531.40 eV (34.35%) associated with oxygen ions located at oxygen vacancy region. The last peak (O_{III}) corresponds to binding energy 533.31 eV (2.13%) represents the adsorbed water content on the surface of the sample [43]. However, the oxygen-related defects in channel layer helps to improve the on-current, and the same may be responsible for leakage current in the dielectric material. Here, in this study, TZO-24 sample possess oxygen-related defect at 531.41 eV (50.42%) and which is comparatively higher than that of ZrO_2 at 531.40 eV (34.35%). Hence, by this XPS analysis, we can expect the minimum leakage current and maximum on-current in ZrO_2/TZO-24-based TFT.

Table 1 XPS spectral peaks of TZO and corresponding atomic percentage concentration

Sample	Zn-2p				Sn-3d				O-1s			
	$2p_{3/2}$ (eV)	Conc. (%)	$2p_{1/2}$ (eV)	Conc. (%)	$3d_{5/2}$ (eV)	Conc. (%)	$3d_{3/2}$ (eV)	Conc. (%)	O_I (eV)	Conc. (%)	O_{II} (eV)	Conc. (%)
TZO-20	1021.46 1023.23	63.75 03.59	1044.56	32.66	486.40	44.90	494.80 498.52	36.17 18.93	529.82	67.41	531.64	32.59
TZO-24	1021.33 1023.04	62.60 02.75	1044.42	33.05	486.30	42.67	494.72 498.34	34.92 22.42	529.55	49.58	531.41	50.42

3.5 Metal–insulator–metal (MIM) studies

The selection of wide bandgap dielectric is essential to create band offset with wide bandgap channel layer, which avoids the carrier injection from gate dielectric to channel layer. In this work large bandgap ZrO_2 films were chosen as a gate dielectric. To study the leakage current density of selected ZrO_2, the MIM structure was constructed, using Al electrodes. The variation in the current density with voltage is displayed in Fig. 9a. To avoid the charging effect, the voltage sweep speed was fixed at 0.1 V/sec [44]. Almost zero offset was noticed in both the curve measured at room temperature and 100 ˚C. The curve exhibited less leakage current densities in the range of 10^{-08} A/cm^2 between the voltage range − 5 V to + 5 V. Similarly, to find the capacitance nature of the ZrO_2, the capacitance–voltage (C–V) measurement (Fig. 9b) was performed at different frequencies for same MIM structure. The average capacitance density was extracted at 10 kHz, 100 kHz, and 1 MHz were 121.9 nF/cm^2, 121.8 nF/cm^2 and 65.0 nF/cm^2, respectively. The dielectric constant of ZrO_2 was calculated by taking the following equation [1]:

$$\boldsymbol{k} = \frac{\mathbf{Cd}}{\boldsymbol{\varepsilon}_0 \boldsymbol{A}} \quad (3)$$

where $\boldsymbol{C}$ is known for capacitance, d indicates the ZrO_2 thickness (120 nm), $\boldsymbol{\varepsilon}_0$ is permittivity of free space, and $\boldsymbol{A}$ is known to be contact area (4.53×10^{-3} cm^2) of the top electrodes. The estimated dielectric constants are 16.52, 16.51 and 8.81 for 10 kHz, 100 kHz, and 1 MHz, respectively. This high dielectric feature considered to be important for excess accumulation of charge carriers at dielectric/semiconductor interface, which lowers the operating voltage of TFTs.

3.6 TFT characteristics

Output characteristics of TZO TFTs at various gate voltages is displayed in Fig. 10a–c. All the devices have exhibited n-channel field effect transistor behaviour and operates in depletion mode. The device clearly indicates a saturation (pinch-off) drain current I_d at lower source–drain voltage (V_{ds}). The channel resistivity was determined from the slope at linear region at $V_{gs} = 0$ V. The estimated values are 28.30 Ω-cm, 3.23 Ω-cm and 0.054 Ω-cm for TZO-20-, TZO-22-, and TZO-24-related TFTs, respectively. All the fabricated devices had shown high output current, and it was found that the order of the current increased from μA to mA as a function of oxygen flow ratio of channel layer. Figure 9d–f indicates the transfer characteristics of TFTs computed at drain–source voltage of 4 V. The source–drain current (I_{ds}) is followed by the relation as follows [44]:

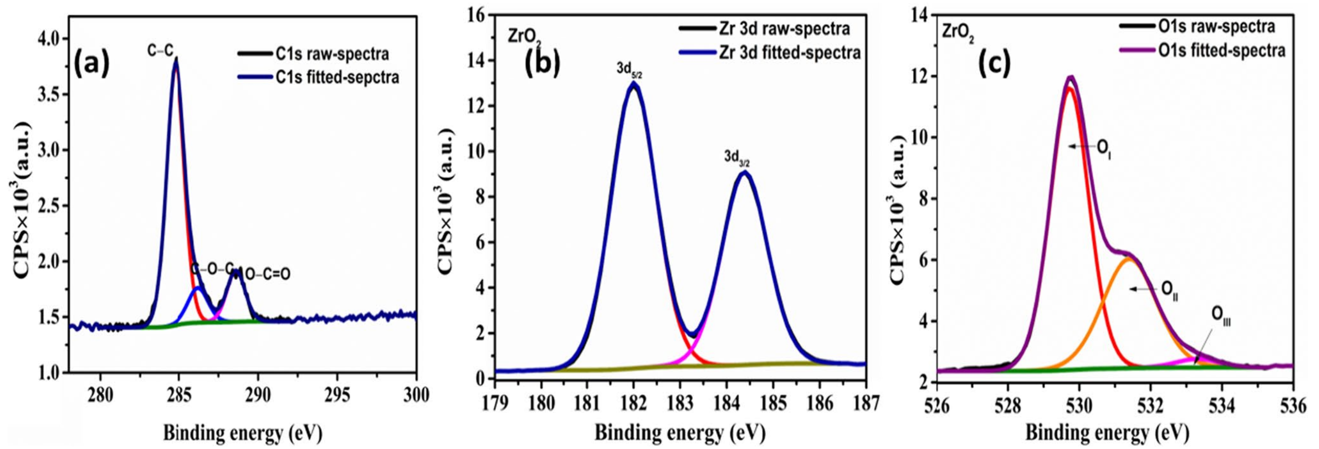

Fig. 8 XPS spectrum of ZrO_2, **a** C1s spectra, **b** Zr 3d spectrum, **c** O1 spectrum of ZrO_2

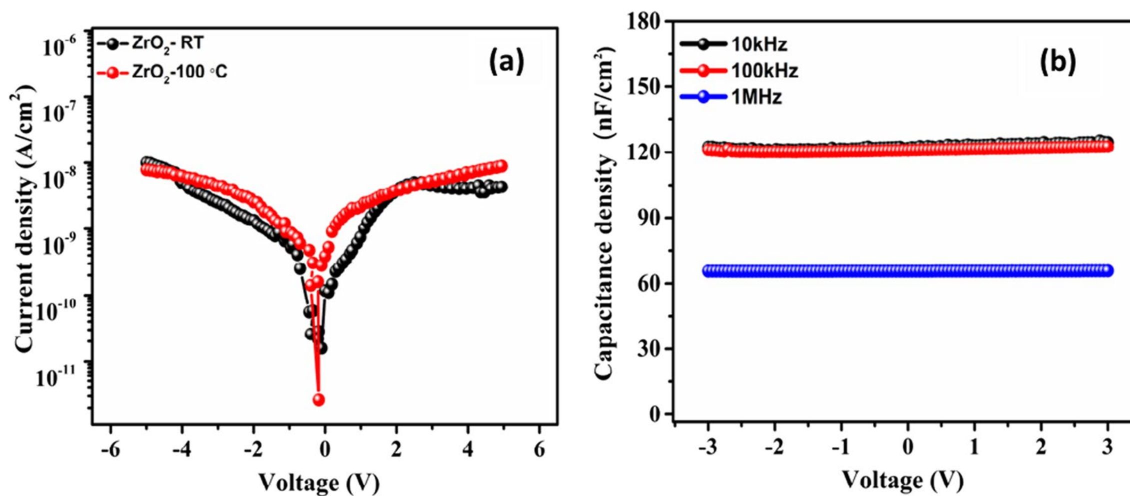

Fig. 9 Al/ZrO_2/Al (MIM) properties, **a** current–voltage measurement of ZrO_2, **b** capacitance–voltage measurement of ZrO_2

$$I_{ds} = \frac{WC_i\mu_{FE}}{2L}\left(V_{gs} - V_T\right)^2 \quad (4)$$

where W, L are width and length of the channels, C_i is the oxide capacitance per unit area, μ_{FE} is the field effect mobility, V_{gs}, V_T are gate–source voltage and threshold voltage, respectively. The threshold voltage of the devices was obtained from x-axis intercept in the $I_{ds}^{0.5}$ versus V_{gs} graph (Fig. 10d–f). The threshold voltage and current on/off ratio were estimated for all the devices and mentioned in Table 2. The betterment in the current on/off ratio (10^2 to $10.^5$) with increase in the oxygen flow ratio for channel layer, which may be due to increase in the oxygen vacancies and good band offset formation as demonstrated by XPS and optical study, respectively. The field effect mobility (μ_{FE}) was derived at low bias of V_{ds} (4 V) and is given by [45]

$$\mu_{FE} = \frac{L}{WC_iV_{ds}}\left(\frac{\partial I_{ds}}{\partial V_{gs}}\right) \quad (5)$$

where L and W are length and width of the channel layer, C_i be the oxide capacitance per unit area, and V_{ds} is the drain voltage (4 V). The filed effect mobility was noticed 7.50×10^{-3} cm^2/V-s, 0.87 cm^2/V-s and 23.31 cm^2/V-s for TZO-20-, TZO-22- and TZO-24-based TFTs. The increment in the field effect mobility is ascribed to high quality interface between ZrO_2 and TZO at higher oxygen flow rate of channel layer because of reduction in the RMS roughness in the TZO films as oxygen flow rate progresses [46]. The subthreshold swing (SS) of the fabricated device can be calculated using the formula [47]:

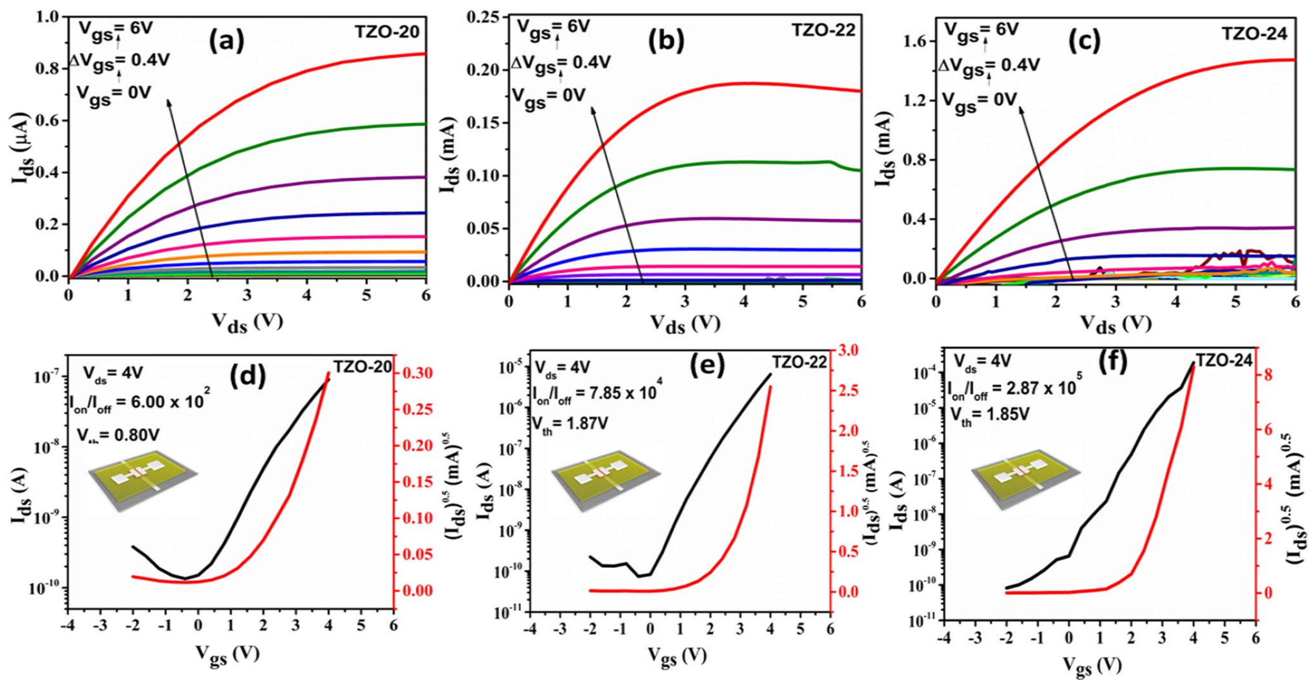

Fig. 10 Electrical parameters of TFTs, **a** output curve of TZO-20-based TFT, **b** output curve of TZO-22-based TFT, **c** output curve of TZO-24-based TFT. **d** Transfer curve of TZO-20-based TFT, **e** transfer curve of TZO-22-based TFT, **f** output curve of TZO-24-based TFT

Table 2 Electrical parameters of thin-film transistors

Devices	Threshold voltage (V_{th}) in V	Current on/off ratio I_{on}/I_{off}	Field effect mobility in μ FE ($cm^2/V.s$)	Subthreshold swing (SS) in V/decade	Surface densities (D_{IT}) in cm^{-2}	Trap densities (N_t) (cm^{-3})	Grain boundary limited mobility μ_{gb} ($cm^2/V.s$)
TZO-20	0.80	6.00×10^2	7.50×10^{-03}	1.78	2.16×10^{13}	1.46×10^{12}	8.71×10^{-03}
TZO-22	1.87	7.85×10^4	0.87	0.91	1.20×10^{13}	1.75×10^{12}	0.625
TZO-24	1.85	2.87×10^5	23.31	0.66	7.95×10^{12}	2.11×10^{12}	76.24

$$\mathbf{ss} = \frac{\mathbf{dV_{gs}}}{\mathbf{d(logI_{ds})}} \tag{6}$$

In this work, the decrease in the SS from 1.78 V/decade to 0.66 V/decade was obtained under the analysis as oxygen flow ratio increased during the channel layer fabrication. Furthermore, to find the surface density of states ($\boldsymbol{D_{IT}}$) at the interface of dielectric/semiconductor, the following formula was used [1]:

$$\boldsymbol{D_{IT}} = \left(\frac{\mathbf{SSlog(e)}}{\mathbf{kT}/\boldsymbol{q}} - 1\right)\frac{\boldsymbol{C_i}}{\boldsymbol{q}} \tag{7}$$

where k is the Boltzmann's constant, e is natural logarithm base, and T indicates absolute temperature, SS is the subthreshold swing, $\boldsymbol{C_i}$ is the capacitance of dielectric material per unit area (121.9 nF/cm^2). From Table 2, we can notice that the computed trap densities found to be decreased as progress in the oxygen flow ratio of the active channel layer (TZO). The higher value of SS and D_{IT} in case of low oxygen flow rated channel layer TFT could be due to dangling bonds presents at the interface between semiconductor–insulator layers, these dangling bonds might be relaxed and formed better interface as increment in the oxygen flow ratio while channel layer coating [48]. We compared the performance of our device with reported work, as mentioned in Table 3.

By analysing XRD results TZO is known to be polycrystalline in nature and found that Levinson's plot is useful to describes the grain boundary limited conduction [44]. Based on this model $\boldsymbol{I_{ds}}$ and $\boldsymbol{V_{gs}}$ are at linear region is related as below:

$$I_{ds} = \mu_{gb} V_{ds} \frac{W}{L} C_i V_{gs} \exp\left(\frac{-q^3 N_t^2 t}{8\epsilon k T C_i V_{gs}}\right) \tag{8}$$

Table 3 Performance evaluation of ZnO-based thin-film transistors

Active layer	Threshold voltage (V_{th}) in V	Current on/off ratio I_{on}/I_{off}	Subthreshold swing (SS) in V/decade	Field effect mobility in μ_{FE} (cm²/V. s)	References
ZnO	1.2	NR	0.13	NR	[20]
ZnO	2.7	10^6	0.5	NR	[50]
ZnO	0.1	10^7	0.06	~37	[43]
Indium zinc oxide	3.22	10^6	0.25	~07	[51]
Zinc–tin–oxide	-0.9	10^6	0.25	~04	[52]
Li-doped ZnO	-1	10^5	NR	~32	[53]
Indium gallium zinc oxide	3.2	NR	0.56	~28	[54]
Tin doped zinc oxide	1.85	10^5	0.66	~23	This work

NR not reported

where N_t is the trap density at grain boundary, μ_{gb} is mobility of carriers at the grain boundary, t is the thickness of the active layer, ϵ is the permittivity of active layer, C_i be the dielectric capacitance density, T is the absolute temperature. By taking the slope of $\ln\left(\frac{I_{ds}}{V_{gs}}\right)$ versus $1/V_{gs}$ plot, the trap density (N_t) can be calculated, and μ_{gb} can be extracted from the intercept. The estimated trap densities are found to be in the order of ~ 10^{12}/cm³ for all the samples. Figure 11a–c displays the $\ln\left(\frac{I_{ds}}{V_{gs}}\right)$ versus $1/V_{gs}$ plot, the computed values are mentioned in Table 2. The maximum μ_{gb} (76.24 cm²/V. s) was observed in the device TZO-24 (i.e., active layer TZO coated at 24% of oxygen flow ratio). By comparing the field effect mobility (μ_{FE}), the grain boundary mobility (μ_{gb}) is nearly three times larger, which depicts that grain boundary traps plays vital role in the transport phenomena of TFTs. From XRD analysis we noticed a slight decrement in the crystallite size with increase in the oxygen flow rate for channel layer coating. It leads to an increase in the grain boundaries and affects the grain boundary limited mobility (μ_{gb}). The computed trap density and μ_{gb} values are good agreement with the results obtained from literature [49].

4 Conclusions

In summary, we have examined the influence of oxygen to argon flow ratio on the properties of co-sputtered TZO thin films synthesized at room temperature. XRD analysis confirmed polycrystalline structure for both the dielectric and active channel layers. AFM analysis showed that increasing the oxygen flow ratio resulted in smoother TZO thin films. Optical analysis revealed over 70% transmittance and improved band offset for TZO and ZrO_2 thin films. XPS analysis revealed an increase in oxygen-related defects and a decrease in zinc interstitials with higher oxygen flow ratio in the active channel. Low leakage current density (10^{-08} A/cm²) and high dielectric constant (~ 16) was confirmed by transport characteristics. The fabricated TFTs operated in the n-channel depletion mode and exhibited good saturation characteristics. Increasing the oxygen flow ratio from 20 to 24% in the channel resulted in a decrease in channel resistivity from 28.30 to 0.054 Ω-cm. The device based on the channel layer synthesized at 24% oxygen flow ratio showed the lowest subthreshold swing of 0.66 V/decade and

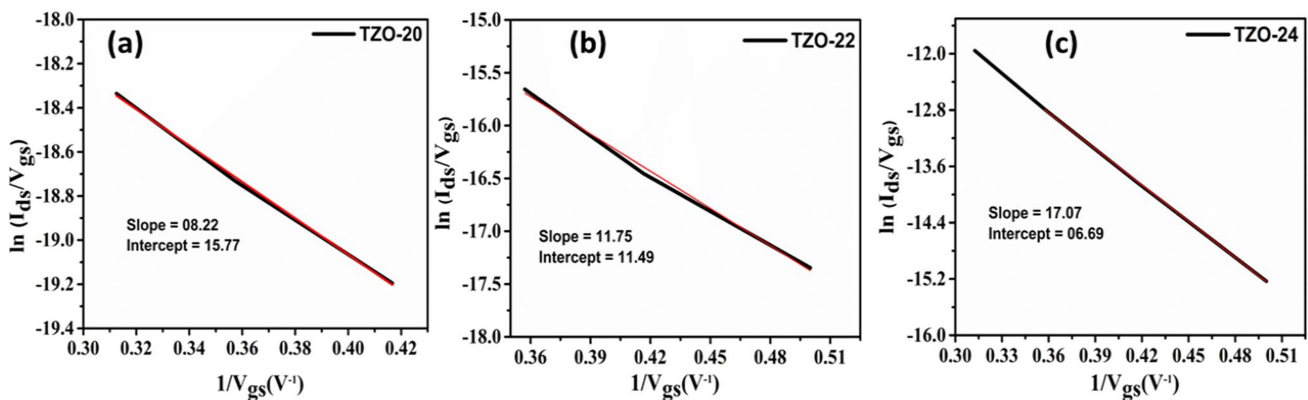

Fig. 11 Levison plots, **a** TZO-20-based TFT, **b** TZO-22-based TFT, **c** TZO-24-based TFT

the highest I_{on}/I_{off} ratio of 10^5. Overall, this work highlights the potential of high-performance, transparent, low-voltage thin-film transistors with low processing temperatures for next-generation smart transparent flexible display applications in various electronic devices.

Acknowledgements The support of this work by the Manipal Academy of Higher Education under the financial assistance of Dr.T.M.A Pai Ph.D. scholarship program. Mr. Prashant Bhat would like to acknowledge Dr. Muhammed Ali for his guidance regarding the electrical analysis part. A part of this research work was accomplished using characterization facilities at CeNSE, Indian Institute of Science Bengaluru, funded by Ministry of Education (MoE), Ministry of Electronics and Information Technology (MeitY), and Nano mission, Department of Science and Technology (DST), Government of India.

Author contributions PB methodology, investigation and writing—original draft. PS validation and data curation. DK: conceptualization and supervision.

Funding Open access funding provided by Manipal Academy of Higher Education, Manipal.

Data availability The data, that supports the findings of this work will be made available on request

Declarations

Conflict of interest The authors declare that they have no known competing financial interests or personal relationships that could have appeared to influence the work reported in this paper.

Open Access This article is licensed under a Creative Commons Attribution 4.0 International License, which permits use, sharing, adaptation, distribution and reproduction in any medium or format, as long as you give appropriate credit to the original author(s) and the source, provide a link to the Creative Commons licence, and indicate if changes were made. The images or other third party material in this article are included in the article's Creative Commons licence, unless indicated otherwise in a credit line to the material. If material is not included in the article's Creative Commons licence and your intended use is not permitted by statutory regulation or exceeds the permitted use, you will need to obtain permission directly from the copyright holder. To view a copy of this licence, visit http://creativecommons.org/licenses/by/4.0/.

References

1. D. Layers, M. Zno, G. Syamala, R. Mullapudi, G.A. Velazquez-nevarez, C. Avila-avendano, R. Ram, J.A. Torres-ochoa, M.A. Quevedo-lo, A.C.S. Appl, Electron. Mater. **6**, 1003 (2019)
2. K.M. Niang, J. Cho, A. Sadhanala, W.I. Milne, R.H. Friend, A.J. Flewitt, Phys. Status Solidi Appl. Mater. Sci. **214**, 1600470 (2017)
3. J.S. Discrete, K. Nomura, H. Ohta, A. Takagi, T. Kamiya **432**, 3383 (2004)
4. G. Wang, B. Chang, H. Yang, X. Zhou, L. Zhang, X. Zhang, S. Zhang, IEEE Electron Dev. Lett. **40**, 901 (2019)
5. Q. Zhang, G. Xia, L. Li, W. Xia, H. Gong, S. Wang, Curr. Appl. Phys. **19**, 174 (2019)
6. W.L. Huang, C.-C. Yang, S.-P. Chang, S.-J. Chang, J. Nanosci. Nanotechnol. **20**, 1704 (2019)
7. W. Hu, R.L. Peterson, Appl. Phys. Lett. **104**, 192105 (2014)
8. H.Q. Chiang, J.F. Wager, R.L. Hoffman, J. Jeong, D.A. Keszler, Appl. Phys. Lett. **86**, 013503 (2005)
9. R.L. Hoffman, Solid State Electron. **50**, 784 (2006)
10. M.G. Mcdowell, R.J. Sanderson, I.G. Hill, M.G. Mcdowell, R.J. Sanderson, I. G. Hill **013502**, 2006 (2013)
11. C. Fernandes, A. Santa, Â. Santos, P. Bahubalindruni, J. Deuermeier, R. Martins, E. Fortunato, P. Barquinha, Adv. Electron. Mater. **4**, 1 (2018)
12. S. Wang, S. Uprety, V. Mirkhani, D. Hanggi, K. Yapabandara, M.P. Khanal, A.C. Ahyi, M.C. Hamilton, M.H. Sk, M. Park, Solid Sate Electron. **191**, 108270 (2022)
13. G.Z. Geng, G.X. Liu, F.K. Shan, A. Liu, Q. Zhang, W.J. Lee, B.C. Shin, H.Z. Wu, Curr. Appl. Phys. **14**, 2 (2014)
14. C. Lee, W. Lee, D. Won, H. Joong, J. Bae, I. Kang, D. Lim, K. Kim, J. Jang, Appl. Surf. Sci. **559**, 149971 (2021)
15. J. Park, J. Won, D. Wook, B. June, H. Jin, J. Sun, Thin Solid Films **518**, 588 (2009)
16. P. Ma, L. Du, Y. Wang, R. Jiang, Q. Xin, Y. Li, Appl. Phys. Lett. **112**, 023501 (2018)
17. M. Esro, G. Vourlias, C. Somerton, W.I. Milne, G. Adamopoulos, Adv. Func. Mater. **25**, 134 (2015)
18. B. Son, S.Y. Je, H.J. Kim, C. Lee, C. Lee, A.Y. Hwang, J.Y. Won, J.H. Song, R. Choi, J.K. Jeong, Phys. Status Solidi (RRL) Rapid Res. Lett. **7**, 485 (2013)
19. C.G. Alvarado-beltra, J.L. Almaral-sa, I. Mejia, M.A. Quevedo-lo, R. Ramirez-bon, ACS Omega **2**, 6968 (2017)
20. K. Kandpal, N. Gupta, J. Singh, C. Shekhar, J. Electron. Mater. **49**, 3156 (2020)
21. M. Takayanagi, D. Nishioka, T. Tsuchiya, M. Imura, Mater. Today Adv. **18**, 100393 (2023)
22. M. Hasan, S. Roy, E. Tokumitsu, H. Chu, S. Chul, J. Jang, Appl. Surf. Sci. **611**, 155533 (2023)
23. C.J. Chiu, Z.W. Pei, S.T. Chang, S.P. Chang, S.J. Chang, Vaccum **86**, 246 (2011)
24. G.F. Li, J. Zhou, Y.W. Huang, M. Yang, J.H. Feng, Q. Zhang **85**, 22 (2010)
25. R. Navamathavan, R. Nirmala, C. Ro, Vaccum **85**, 904 (2011)
26. K. Ellmer, J. Phys. D. Appl. Phys. **33**, R17 (2000)
27. P. Bhat, P. Salunkhe, D. Kekuda, Phys. E Low-Dimens. Syst. Nanostruct. **149**, 1 (2023)
28. P. Bhat, P. Salunkhe, D. Kekuda, Sens. Actuat. A Phys. **354**, 114279 (2023)
29. M.A. Islam, K.S. Rahman, F. Haque, N.A. Khan, M. Akhtaruzzaman, M.M. Alam, H. Ruslan, K. Sopian, N. Amin, J. Nanosci. Nanotechnol. **15**, 9184 (2015)
30. P.J. Kelly, R.D. Arnell, Vacuum **56**, 159 (2000)
31. P. Bhat, P. Salunkhe, M.S. Murari, D. Kekuda, Phys. B Condens. Matter **628**, 413571 (2021)
32. S. Zinatloo-ajabshir, M. Salavati-niasari, J. Mol. Liq. **216**, 545 (2016)
33. P. Bhat, P. Salunkhe, M.S. Murari, D. Kekuda, Sens. Actuat. A Phys. **338**, 113479 (2022)
34. X. Xu, Y. Chen, G. Zhang, H. Bian, M. Zhao, S. Ma, Superlattices Microstruct. **123**, 349 (2018)
35. G. Greczynski, L. Hultman, Sci. Rep. **11**, 90780 (2021)
36. N. K. S. A. Kumar, R. D. S. Jena, A. K. V. R. Singh, and R. S. D. Panda, J. Electron. Mater. **52**, (2022)
37. N. Mahdi, P. Kumar, A. Goswami, B. Perdicakis, K. Shankar, Nanomaterials **9**, 1186 (2019)
38. A. Murali, H.Y. Sohn, J. Mater. Sci. Mater. Electron. **29**, 14945 (2018)
39. K.J. Chen, F.Y. Hung, Y.T. Chen, S.J. Chang, Z.S. Hu, Mater. Trans. **51**, 1340 (2010)
40. L. Chao, S. Lin, W. Chang, Nucl. Inst. Methods Phys. Res. B **268**, 1581 (2010)

41. S. Dhara, K.M. Niang, A.J. Flewitt, A. Nathan, S.A. Lynch, Sci. Rep. **11**, 19016 (2021)
42. A. Chen, K. Zhu, H. Zhong, Q. Shao, G. Ge **120**, 157 (2014)
43. J. Yang, Y. Zhang, Q. Wu, C. Dussarrat, J. Qi, W. Zhu, IEEE Trans. Electron Dev. **66**, 3382 (2019)
44. Dhananjay, S.B. Krupanidhi, J. Appl. Phys. **101**, 123717 (2007)
45. P. Heremans, A.K. Tripathi, A.D.J. De Meux, E.C.P. Smits, B. Hou, G. Pourtois, G.H. Gelinck, Adv. Mater. **28**, 4266 (2016)
46. R.N. Bukke, C. Avis, M.N. Naik, J. Jang, IEEE Electron Dev. Lett. **39**, 3106 (2018)
47. P. Braga, G. R. De Lima, G. R. De Lima, G. Gozzi, J. P. Braga, L. F. Santos, L. F. Santos, Dhanasekaran Vikraman (Eds.), Hyun-Seok Kim, Intech Open., pp 135–145 (2018)
48. Y. Li, X. Zeng, Q. Ye, R. Yao, J. Zhong, X. Fu, Y. Yang, M. Li, H. Ning, J. Peng, Surf. Interfaces **33**, 102184 (2022)
49. M.A.V. Ali, D. Kekuda, Phys. Status Solidi (a) **214**, 1700113 (2017)
50. B. Walker, A.K. Pradhan, B. Xiao, Solid. State. Electron. **111**, 58 (2015)
51. J.H. Park, Y.B. Yoo, K.H. Lee, W.S. Jang, J.Y. Oh, S.S. Chae, H.K. Baik, A.C.S. Appl, Mater. Interfaces **5**, 410 (2013)
52. A.T. Oluwabi, A. Katerski, E. Carlos, R. Branquinho, A. Mere, M. Krunks, E. Fortunato, L. Pereira, I. Oja-Acik, J. Mater. Chem. C **8**, 3730 (2020)
53. G. Adamopoulos, S. Thomas, P.H. Wöbkenberg, D.D.C. Bradley, M.A. McLachlan, T.D. Anthopoulos, Adv. Mater. **23**, 1894 (2011)
54. J.S. Lee, S. Chang, S.M. Koo, S.Y. Lee, IEEE Electron Dev. Lett. **31**, 225 (2010)

Publisher's Note Springer Nature remains neutral with regard to jurisdictional claims in published maps and institutional affiliations.